Transactions of the SMiRT 27
Yokohama, Japan, March 3-8, 2024
Division II

Microstructural evolution of selective laser melted 316L under low cycle fatigue loadings at 550 ℃ high temperature

Xiaowei Wang[1], Yefeng Chen[2], and Jianming Gong[3]

[1] Professor, Nanjing Tech University, Nanjing, China(xwwang@njtech.edu.cn)
[2] PhD student, Nanjing Tech University, Nanjing, China(chenyf@njtech.edu.cn)
[3] Professor, Nanjing Tech University, Nanjing, China(gongjm@njtech.edu.cn)

ABSTRACT

As a realistic alternative to many conventional manufacturing techniques, selective laser melting (SLM) has attracted much attention in nuclear field due to numerous advantages. The 316L stainless steel is widely used in nuclear plants due to its excellent corrosion resistance and good high temperature mechanical properties. To ensure the integrity of SLM 316L components under low cycle fatigue (LCF) loading which is common in nuclear field, the microstructural evolution and fatigue of SLM 316L under LCF loading are investigated. In this study, a set of LCF tests for SLM 316L at 550 ℃, which is the typical operation temperature of sodium-cooled fast reactor in generation IV nuclear plants. Results show that SLM 316L has higher strength (YS 568 MPa and UTS 693 MPa) and lower ductility (elongation 52%) compared with traditional 316L. The high strength is mainly attributed to the (i) cellular substructure, (ii) high dislocation density, and (iii) high content of LAGB, formed by the high cooling rate. SLM 316L has better LCF properties than traditional 316L, shown in Fig. 1. It has longer life at 0.3, 0.4 and 0.6% strain amplitudes and similar life at 0.8 and 1.0% strain amplitudes. It has significantly higher stress amplitude (cyclic strength) than traditional 316L and more stable cyclic (softening) behavior which is beneficial for engineering applications. The cyclic softening behavior of SLM 316L is mainly attributed to: (i) coarsening of the cellular sub-structure, (ii) texture evolution from <111>∥LD to <001>∥LD, shown in Fig. 2, and (iii) decrease of GND density and LAGBs during fatigue. A transgranular fracture mode is observed across a range of strain amplitudes in SLM 316L. At higher strain amplitudes, fatigue cracks are fewer, shorter and wider. The melt boundaries have no obvious effect on resistance or promotion of crack propagation. Fatigue cracks originate from lack-of-fusion defects near the surface of all strain amplitudes. At lower strain amplitudes (0.4%), oxide layer can also act as crack initiation sites. The propagation direction for fatigue cracks is parallel to the build direction due to columnar grains in the microstructure. In addition, a *P*-*ε*-*N* prediction approach based on small sample set is proposed to evaluate the reliability of SLM 316L at different strain amplitude.

1. INTRODUCTION

Since the 316L was first printed by Kruth in 2003, most research has focused on tensile and HCF (high cycle fatigue) behavior and properties. In terms of tensile properties, SLM 316L can achieve an excellent balance between strength and ductility through SLM technology (Wang et al. 2018). The high strength of SLM 316L is attributed to the fine sub-structure, high dislocation density, very low-angle grain boundaries, and dispersive nano-oxides formed by the high process cooling rates. However, anisotropy, hierarchical features and defects of SLM 316L have a significant influence on fatigue property. Firstly, SLM 316L has anisotropic properties due to grain growth along the build direction. Wood et al. (Wood et al. 2019)investigated the influence of build orientation on fatigue strength, and found that horizontally-printed specimens have 20%-45% higher fatigue strength than vertically-printed specimens due to the higher tensile strength and smaller surface roughness of the former. Stern et al. (Stern et al. 2019)reached a similar conclusion that vertically printed specimens have weak bonding between layers and lower resistance to crack growth. The loading direction, which in turn depends on the build direction, affects crack growth path and rate. Secondly, the hierarchical feature of SLM 316L has a significant influence on fatigue performance. Hatami et al. (Hatami et al. 2020) discovered that layer thickness has a minor negative impact on fatigue strength, however it has a significant effect on the production efficiency. Also, the direction and thickness of layers affect crack growth paths and rates. Thirdly, defects, which are a dominant feature of SLM 316L, have an adverse influence on fatigue properties. Defects in SLM can be divided into surface and internal defects. Surface defects are mainly surface roughness and surface pores. As many previous studies have shown, specimens after machining or electropolishing (Andreau et al. 2021; Benedetti et al. 2017) have significantly higher fatigue properties than as-built specimens because surface pores have a significant detrimental effect on HCF strength. Regarding internal defects, including key holes, gas pores, and lack of fusion, among which lack of fusion is more dangerous for fatigue loading due to its large volume and sharp shape. Compared

with internal defects in the core, internal defects in the sub-surface have a larger effect on fatigue strength and life cycles. Hence, various methods of process parameter optimization and post heat treatment, like annealing and hot isostatic pressing, have been developed for reducing internal defects or increasing defect tolerance (Blinn et al. 2020). To date, little research has been conducted on deformation mechanisms of additively manufactured stainless steel. Zhang et al. (Zhang et al. 2021) demonstrated that HCF loading promotes local recrystallization of SLM 304L at room temperature. The recrystallization behavior, in turn, in the overlap area, has a detrimental effect on fatigue performance by weakening resistance to fatigue crack initiation. For LCF loading at room temperature, twin boundaries act as sites for crack initiation in SLM 304L (Pegues, Roach, and Shamsaei 2019). Most studies on fatigue of SLM material are focused on HCF behavior at room temperature. To the authors' knowledge, little research has been presented on deformation mechanisms and LCF behavior for SLM 316L at high temperature.

In addition, the SLM materials usually exhibit great dispersion in fatigue properties compared against the conventional ones due to random defects and unstable process parameters. The reliability analysis of fatigue life is an essential method to evaluate the uncertainty. The ε-N curves (strain-fatigue life) that indicate the fatigue limit of materials are the most important references for engineering design. Nevertheless, the predictive value derived from fitting a line between ε-N scatter plots exhibits a survival probability of only 50%. Safety factors has been extensively employed in several design standards to mitigate the occurrence of unforeseen fatigue failure. However, it also results in a significant reduction in residual bearing capacity. In order to meet the different demands on reliability during service, the P-ε-N curves have been presented. Considering LCF test requires a lot of time and economic consumption, the dataset of LCF is very limited (Xie et al. 2014). The scale of life data of single strain amplitude is very small, usually 2 or 3 data points are available. However, the traditional method to quantitatively describe the probabilistic variation is to do probability fitting using approximately 15 specimens at each of the four or five constant stress levels. Consequently, there is a need for a reliability analysis method that is applicable to small sample size to improve the accuracy of LCF reliability assessment.

This study is mainly focused on the microstructural evolution and reliability assessment of SLM 316L under LCF loading. First, a series of LCF tests at various strain amplitudes is conducted on SLM 316L and traditional 316L to examine the comparative performance. The specific cyclic softening behavior of SLM 316L is investigated from the aspect of microstructure evolution. In addition, the influence of the strain amplitude on the development and propagation of fatigue cracks is examined. Last but not least, a new method based on Weibull distribution model is applied to estimate the P-S-N curves, in which the remora optimization algorithm (ROA) is first introduced to calculate the values of characteristic parameters.

2. EXPERIMENTAL DETAILS

The SLM specimens for investigation were manufactured in a controlled environment with 99.999% argon gas using the SLM 125HL (SLM Solutions GP, Germany) equipped with a 400 W fiber laser. The following commercial standard process parameters are used: laser power (P) = 200 W, scanning speed (V) = 800 mm/s, layer thickness (t) = 30 μm, hatch distance (H) = 120 μm, pre-heat temperature (T_{pr}) = 100 ℃. The size distribution of the gas-atomized powder ranges from 10 to 45 μm, and the nominal chemical composition (in wt.%) is shown in Table 1. By using Archimedes method, the relative density of the SLM 316L was found to be greater than 99.3%, which meets the ASTM F3184-16 standard. It is worth noting that the specimens subjected to final testing are machined and polished from blocks, as depicted in Figure. 1(a). Prior to conducting the fatigue tests, the surface of the specimen gauge length is meticulously polished to achieve a surface roughness (Ra) of less than 0.2 μm. Fig. 1(b) illustrates the geometry of the test specimen for SLM 316L.

Table 1 Chemical compositions of materials (wt.%)

Composition	Fe	Cr	Ni	Mo	Mn	Si	P	S	C	N
316L powder	Balance	16-18	10-14	2-3	2.00	1.00	0.045	0.03	0.03	0.100
SLM 316L	Balance	18.46	12.49	2.4	0.74	0.75	0.025	0.012	0.040	0.054

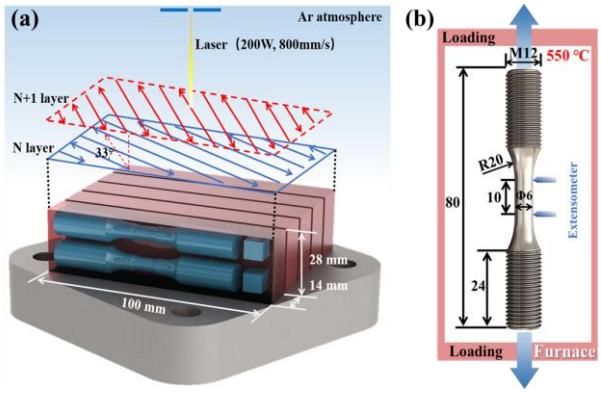

Fig. 1 (a) Schematic of scanning strategy and specimen position; (b) definition of specimen geometry.

A series of fully-reversed axial strain-control tests was performed with a constant strain rate of $1.0\times10^{-3}s^{-1}$ at 550 ℃, for total strain amplitude ε_t of 0.25 %, 0.3 %, 0.4 %, 0.6 %, 0.8 % and 1.0 %. The temperature was measured by three K-type thermocouples near the gauge section. A 10 mm gauge extensometer produced by Epsilon was used to measure the deformation. All experimental data (stress, strain, time, etc.) are collected by EDC220 controller according to the specified time interval. The test conditions and fatigue life data in the present work are listed in Table 2.

Table 2 Fatigue life of SLM 316L.

Temperature (℃)	Total strain amplitude, ε_t (%)	Fatigue life, N_f (cycles)	Total strain amplitude, ε_t (%)	Fatigue life, N_f (cycles)
550	0.25	8600	0.6	1225
550	0.25	15370	0.6	916
550	0.3	12450	0.6	1513
550	0.3	8166	0.8	433
550	0.3	10457	0.8	391
550	0.4	4017	0.8	634
550	0.4	5000	1.0	319
550	0.4	2448	1.0	240

3. RESULTS

3.1 Microstructural characterization

Fig. 2(a) shows the representative microstructure in SLM 316L. As shown in Fig. 2(a), SLM 316L has a hierarchical and finger-shaped formation due to the layer-by-layer and track-by-track melting method. The melt pool boundaries (red line in Fig. 2(a)) are attributed to the laser track and the powder layer. Its width and depth are dependent on laser diameter and thickness of the powder layer, respectively. The area surrounded by the blue line is the remelt zone which is intersected by two adjacent melt pools in the same layer. From Fig. 2(a), a very fine sub-structure is observed within the melt pool. The sub-structure has two shapes of columnar and cellular structures from different views.

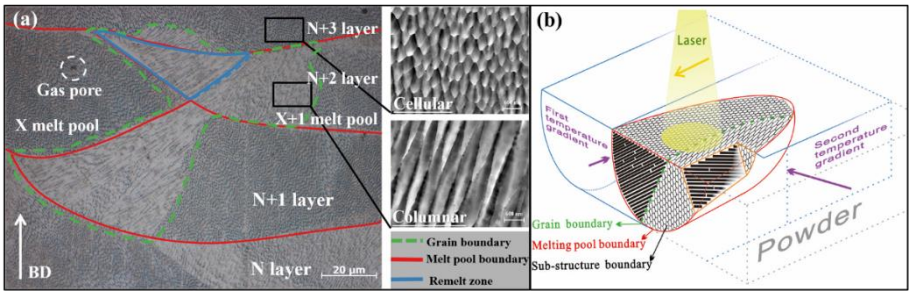

Fig.2 (a) Microstructure of SLM 316L (BD: build direction); (b) The schematic of cellular sub-structure growth.

Fig. 3 displays a representative grain orientation map and misorientation angle distribution for SLM 316L in as-built condition. It is observed that many columnar and complex grains are distributed in SLM 316L. The grains grow along the build direction, which corresponds to the temperature gradient between layers. The melt pool boundary and powder layer can't be observed in the EBSD map,

indicating that the melt pool boundary and powder layer have no obvious influence on the growth of grains and sub-structure. In addition, the cellular sub-structure cannot be identified from the EBSD orientation map, proving that the cellular sub-structure has same crystallographic orientation. From Fig. 3(b), it can be seen that SLM 316L has a large fraction (about 79%) of LAGB, with misorientation less than 10°.

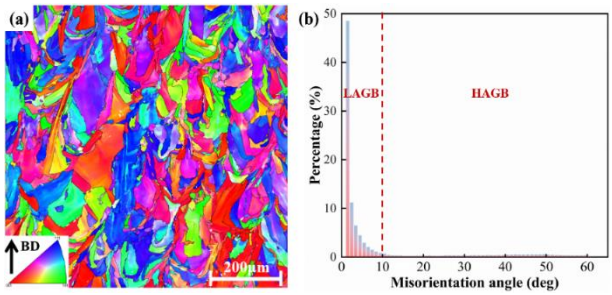

Fig. 3 EBSD analysis of SLM 316L: (a) Grain orientation map; (b) histogram of misorientation angle distribution.

3.2 Tensile properties

Fig. 4 shows the measured engineering stress-strain curves of both SLM 316L and traditional 316L, and the tensile properties results of 0.2% offset yield strength (YS), ultimate tensile strength (UTS) and elongation are listed in Table 2 with additional comparative data. The stress-strain curve of the traditional 316L exhibits a quite wide region of work hardening after yielding (289 MPa) until the UTS (589 MPa) is reached at the maximum uniform elongation (UE) of 62%. The tensile stress then drops till fracture occurs at a tensile elongation of 92%. The YS of SLM 316L is 568 MPa, which is 96.5% higher than that of traditional 316L. After yielding, the tensile stress reaches the UTS rapidly with a narrow region of work hardening. The 52% elongation of SLM 316L is much lower than 93% elongation of traditional 316L, is still higher than the standard value 35% for wrought material.

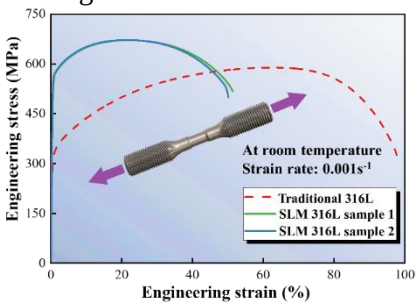

Fig. 5 Measured stress-strain curves of SLM 316L and traditional 316L.

3.3 Fatigue properties

The LCF life scatters of SLM 316L are shown in Fig. 6. According to the ASTM standard, the logarithmic linear fitting ε-N curve is obtained by the Basquin relationship. From Fig. 6, a larger scattering of fatigue lives can be observed. In order to describe the scattering of fatigue lives, the probability (or reliability) need to be analyzed.

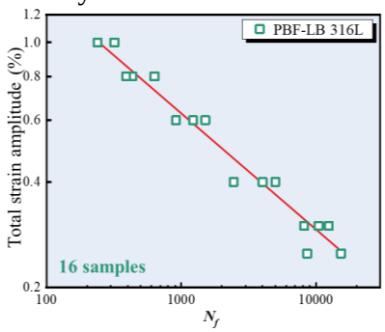

Fig. 6 LCF life scatters of SLM 316L.

3.4 Crack propagation and fracture morphology

Fig. 7(a-c) shows typical transgranular cracks under different amplitudes in traditional 316L. The fatigue cracks originate from the surface and subsequently propagate into the core of the specimens. As

is shown in Fig. 7(g), for lower strain amplitudes, e.g. 0.4 %, most plastic deformation is concentrated in a persistent slip band and a crack is nucleated at the intersection of the surface and a slip band. Fig. 7(h) shows that the grain boundary near the surface is torn open and a crack nucleates due to larger plastic deformation when the strain is higher (0.8%). Generally, the higher the strain amplitude, the fewer and shorter the fatigue cracks.

Similarly, transgranular fracture is observed in SLM 316L at different strain amplitudes. Fig. 7(d-f) shows that columnar grains are widely distributed in SLM 316L. The cracks originate from the surface and propagate into the core of the specimens. The crack initiation locations seem to be randomly distributed on the surface. Strain amplitude has a significant influence on crack length. At higher strain amplitudes, shorter cracks are observed. In addition, the melt pool boundary appears to have no obvious effect on crack propagation.

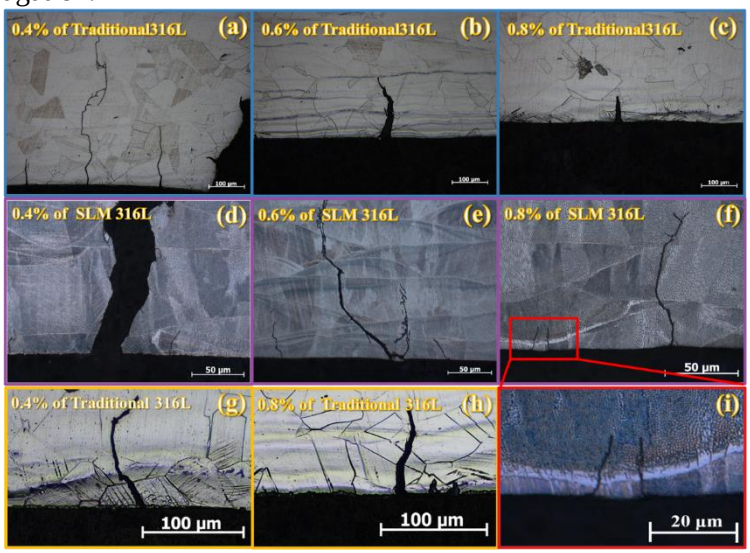

Fig.7 Crack path in the vicinity of fracture surface: (a-c) traditional 316L at 0.4, 0.6, 0.8% strain amplitude; (d-f) SLM 316L at 0.4, 0.6, 0.8% strain amplitude; (g) crack originated at the intersection of surface and a slip band; (h) crack originated at the grain boundary; (i) the crack paths across the melting boundary.

Three representative specimens after LCF tests at strain amplitudes of 0.4%, 0.6%, and 0.8% are chosen for investigation of the morphology of fracture surface, the SEM images of which are shown in Fig. 8. The fatigue crack initiation sites and crack growth regions are characterized by a radial flow pattern, whereas the final fracture zone exhibits typical ductile fracture. As shown, the numbers of fatigue crack initiation sites are 5, 2, and 1 for the 0.4%, 0.6%, and 0.8% cases, respectively. With increase in strain amplitude, the number of crack initiation sites decreases. This is consistent with the results of the OM analysis. From the fracture, lack-of-fusion defects are observed near the surface. As is shown in Fig. 8(e)(f)(h)(i)(k)(l), the fatigue cracks initiate from the lack-of-fusion defects near the surface at 0.4, 0.6 and 0.8%strain amplitudes. When strain amplitude is 0.4%, a closer observation shows that the crack also initiates from the sub-surface of the oxide layer (Fig. 8(b), (c)). The figure with a green border in Fig. 8(d) clearly shows many striations and fine oxide particles adhere to the fatigue striations at 0.4% strain amplitude. The oxidation effect can't be ignored during fatigue crack propagation. As is shown in Fig. 8(m-o), secondary cracks can be observed during the propagation of fatigue cracks.

As is shown in Fig. 9, SLM 316L exhibits a typical cyclic softening behavior at different strain amplitudes, whereas, in contrast, traditional 316L exhibits cyclic hardening behavior. In traditional 316L, the material shows initial hardening, saturation and rapid softening. The degree of hardening is found to be dependent on strain amplitude, increasing with strain amplitude. Compared with the rapid increase and decrease of peak tensile stress in traditional 316L, SLM 316L has a more stable cyclic behavior, which is beneficial for engineering applications. It is noting that SLM 316L exhibit initial cyclic hardening in few cycles at 0.8% and 1.0% strain amplitude.

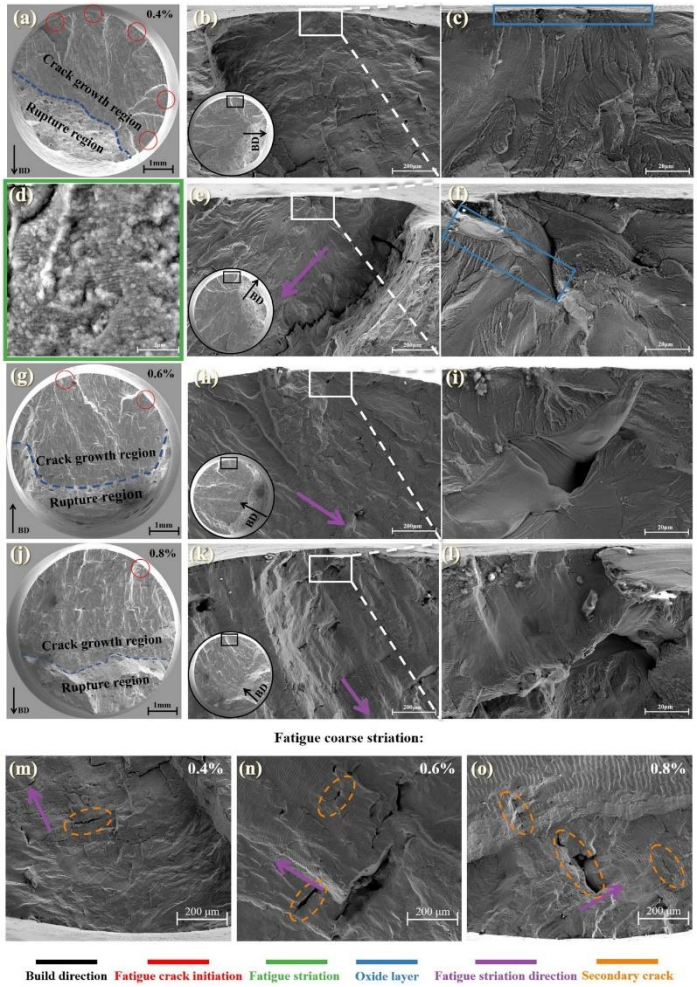

Fig. 8 The fracture morphology of SLM 316L: (a-c, e-f) 0.4%; (d) oxide characterization of 0.4% LCF; (g-i) 0.6% LCF; (j-l) 0.8% LCF; (m-o) secondary crack and fatigue striation direction of 0.4, 0.6, and 0.8% respectively.

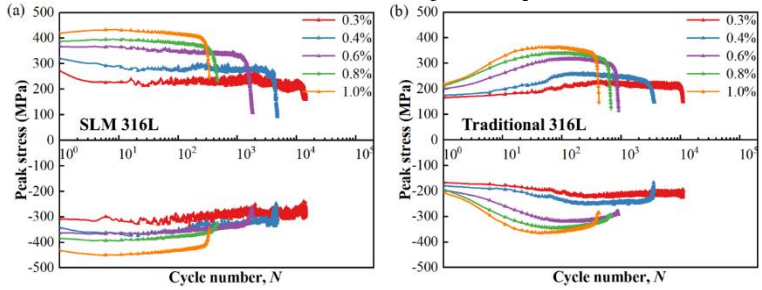

Fig. 9 Peak stress curves of (a) SLM 316L and (b) traditional 316L at different strain amplitudes.

4. DISSCUSSION

4.1 Microstructural evolution

Fig. 10 shows the coarsening of the cellular sub-structure after fatigue loading and high-temperature aging. The evolution of the cellular sub-structure therefore can be expected to affect the cyclic deformation behavior under LCF conditions. From the OM images, the diameter of cellular structure in as-built SLM 316L is 0.707 ± 0.078 μm. As shown in Fig. 10, the size of the sub-structure is 0.709 ± 0.039 μm after aging at 550℃ for 325 h. This indicates that the sub-structure has excellent thermal stability at the high temperature of 550℃. However, fatigue loading has a significant influence on the cellular sub-structure. The diameter of the cellular sub-structure grows to 0.73 ± 0.064 μm, 0.75 ± 0.061 μm and 0.82 ± 0.087 μm after 0.4%, 0.6% and 0.8% strain amplitude respectively.

This sub-structure coarsening leads to cyclic softening. Pham et al. [23] identified a Hall-Petch relationship between yield strength and size of sub-structure. So, sub-structure coarsening directly leads to decrease of yield stress during fatigue loading, obviously causing the cyclic softening in SLM 316L.

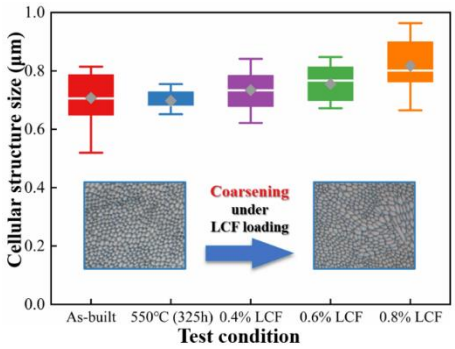

Fig. 10 The evolution of cellular sub-structure in different conditions.

Fig. 11(a-c) show the grain orientations of the as-built, 0.4% and 0.8% fatigued samples. Fig. 11(d-f) are inverse pole figures which used Exp. Densities to reflect the distribution frequency of grain orientations in the analyzed areas. Fig. 11(d-f) show obvious concentration of grain orientations and exhibit obviously different textures along the loading direction (LD) in as-built and post-test fatigue samples. It is noticeable from Fig. 11(a) that the microstructure consists of a mixture of fine, coarsen and columnar grains. The columnar grains are generally parallel to the build direction. So, the as-built sample shows <111>∥LD, and <001>∥LD texture in Fig. 11(d). From Fig. 11(e-f), the <111>∥LD disappeared, and the intensity of <001>∥LD increased with the increasing of strain amplitude. So, it is concluded that the <111>∥LD texture transforms into <001>∥LD texture after cyclic LCF loading. For FCC (face-centered cubic) materials, texture direction directly influences tensile properties. Compared with <111>∥LD texture, <001>∥LD texture has lower yield stress and elongation due to different Schmid factors (Wang et al. 2019). And, the maximum value of the elastic modulus of FCC is obtained along the <111> direction and the minimum along <001> direction. In summary, the texture evolution from <111>∥LD to <001>∥LD leads to the decreasing of yield stress during cyclic loading in SLM 316L.

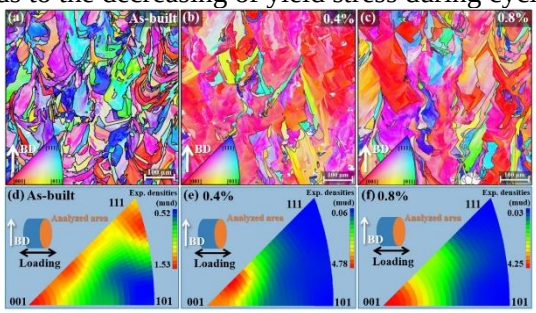

Fig. 11 EBSD inverse pole figure (IPF) orientation maps of (a) as-built, (b) 0.4% LCF, and (c) 0.8% LCF; Inverse pole figure (IPF) of (d) as-built, (e) 0.4% LCF, and (f) 0.8% LCF.

Fig. 12 shows the GND density maps of the as-built and post-fatigue samples. The GND is heterogeneously distributed. The average density of GND is $7.54\times10^{14}/m^2$ for as-built SLM 316L. After the cyclic loading at the strain amplitudes of 0.4 and 0.8%, the GND densities reduce to $4.89\times10^{14}/m^2$ and $4.48\times10^{14}/m^2$ respectively. As a result, the stress required for dislocation movement decreased, leading to cyclic softening.

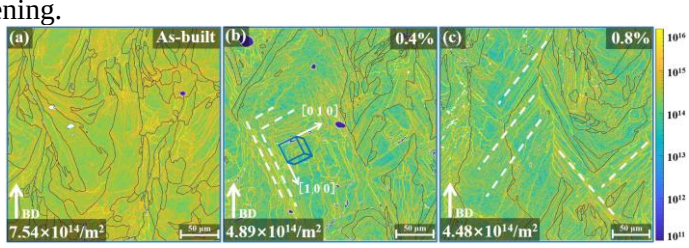

Fig. 12 Geometrically necessary dislocation distribution of (a) as-built, (b) 0.4%, and (c) 0.8% LCF.

In addition, Fig. 13(a) shows the distribution of misorientation angle among grains. The occurrence of HAGBs which includes critical grain boundary angle (15° usually) decreases after fatigue loading. As is shown in Fig. 13(b), grain size (equivalent diameter) also increases slightly after low cycle fatigue loading. The decreasing of HAGBs is closely related to grain coarsening. However, the so sight coarsening of grains (about 1μm difference) is less likely to cause cyclic softening. The occurrence of LAGBs in as-built 316L is about 3.13×105, decreasing to 1.23×10^5 and 1.12×10^5 after testing at 0.4%

and 0.8% strain amplitudes, respectively. The annihilation of LAGBs during fatigue loading reduces the contribution to yield strength (Kurzynowski et al. 2018), leading to the observed cyclic softening.

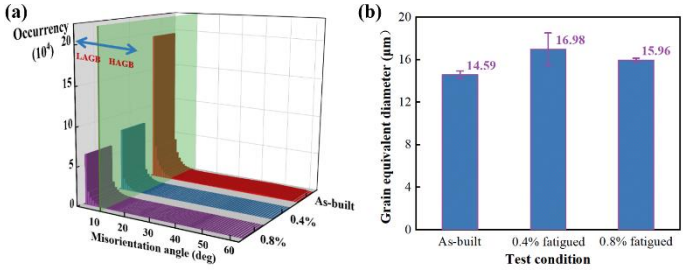

Fig. 13 (a) Misorientation angle distribution, and (b) grain diameter of as-built, 0.4 and 0.8% post-fatigue SLM 316L samples.

In summary, the cyclic softening behavior of SLM 316L can be contributed to these evolutions of microstructure: (i) coarsening of the cellular sub-structure, (ii) texture evolution from <111>∥LD to <001>∥LD, and (iii) decrease of GND density and LAGBs during fatigue.

4.2 Reliability assessment

In LCF performance of AM material, the Basquin model is also suitable for describe the relationship between strain (ε) and fatigue life (N) (Concli et al. 2021; Wu et al. 2010; Zhang et al. 2022). Moreover, the total strain amplitude ε_t is denoted by a combination of elastic strain ε_e and plastic strain ε_p, forming the Coffin-Manson-Basquin model:

$$\varepsilon_t = \varepsilon_e + \varepsilon_p = \frac{\sigma_f^{'}}{E}(2N_f)^b + \varepsilon_f^{'}(2N_f)^c \tag{1}$$

where σ'_f is the fatigue strength coefficient, E is the Young's modulus, b is the fatigue strength exponent, ε'_f is the fatigue ductility coefficient and c is the fatigue ductility exponent. The Coffin-Manson-Basquin model can be easily divided into two parts and transformed into linear expression:

$$\begin{aligned} \log(\varepsilon_e) &= \mathrm{Log}(\frac{\sigma_f^{'}}{E}) + b\log(2N_f) \\ \log(\varepsilon_p) &= \mathrm{Log}(\varepsilon_f^{'}) + \mathrm{c}\log(2N_f) \end{aligned} \tag{2}$$

To simplify the model description, proper parameter transformations are given as:

$$\begin{aligned} \log(2N_f) &= -\frac{1}{b}\log(\frac{\sigma_f^{'}}{E}) + \frac{1}{b}\log(\varepsilon_e) = a_e + b_e\log(\varepsilon_e) \\ \log(2N_f) &= -\frac{1}{c}\log(\varepsilon_f^{'}) + \frac{1}{c}\log(\varepsilon_p) = a_p + b_p\log(\varepsilon_p) \end{aligned} \tag{3}$$

Eq. (11) indicates that both ε_e and ε_p exhibit linear relationships with the fatigue life. Therefore, they can be expressed by a generalized equation to facilitate the description (Wen et al. 2019):

$$\log(2N_f) = a_o + a_1\log(\varepsilon_t) \tag{12}$$

where a_0 and a_1 are constants to denote the intercept and slope of liner relationship. So far, the Basquin model between N_f and ε_t in LCF has been proposed. Through patterning the analysis procedure in HCF mention in Section 2.1, the PDF and MLE cost function can be easily expressed as following:

PDF:

$$\begin{aligned} &f(N) = \frac{\beta}{\eta}\cdot\left(\frac{N}{\eta}\right)^{\beta-1}\cdot\exp\left[-\left(\frac{N}{\eta}\right)^{\beta}\right];\ N,\beta,\eta>0 \\ &\eta = 10^{a_0+a_1\log(\varepsilon_t)};\ a_0>0,\ a_1<0 \\ &\beta = const;\ \beta>0 \end{aligned} \tag{4}$$

MLE cost function:

$$MLE(a_0,a_1,\beta) = \sum_{i=1}^{n}\left\{\ln\left[f(N_i|\varepsilon_{t,i})\right]\right\} = \sum_{i=1}^{n}\left\{\ln\left(\frac{\beta}{\eta}\cdot\left(\frac{N_i}{\eta}\right)^{\beta-1}\cdot\exp\left(-\left(\frac{N_i}{\eta}\right)^{\beta}\right)\right)\right\} \tag{5}$$

To further validate the usability of SLM 316L in engineering, the LCF reliability are compared between traditional 316L SLM 316L. The LCF life data of traditional 316L are all achieved from 316L material and same test conditions. By the newly proposed method, the $N_{5\%}$, $N_{50\%}$ and $N_{95\%}$ curves of

traditional 316L are calculated and shown in Fig. 14. Compared with tradition 316L, the LCF life data of SLM 316L has larger scattering range. This dispersion exhibits the unstable fatigue properties, which is mainly attributed to internal defects in SLM 316L (Kumar et al. 2020). Fig 14 also shows that there are transection points on $N_{50\%}$ and $N_{95\%}$ curves of traditional and SLM 316L, indicating the LCF performance superiority is also affected by the strain amplitude. When the strain amplitude is higher than these transection points, the traditional 316L has longer LCF lives. However, the SLM 316L has better LCF performance when the strain amplitudes are lower than transection points. This phenomenon is similar to result in our previous research (Chen et al. 2022). Compared to the traditional 316L, the SLM 316L exhibits higher strength but lesser ductility (Wang et al. 2018). The higher strength offers the SLM 316L higher elastic limit, which represent capacity to tolerate small strain deformation (Elangeswaran et al. 2019). However, the LCF properties of SLM 316L get worse because it is dominated by the plastic deformation at high strain amplitude.

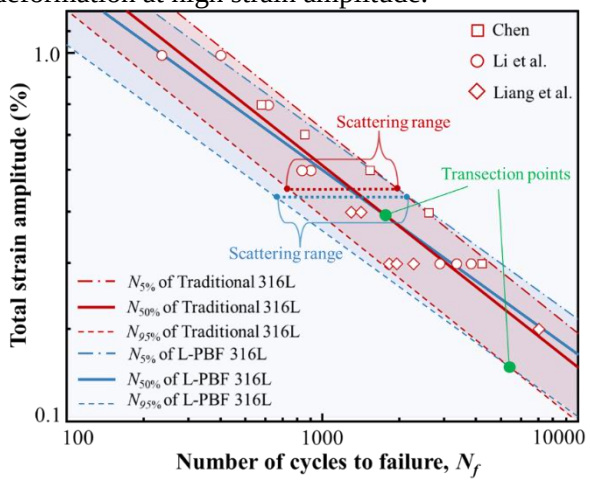

Fig. 14 LCF properties comparison between traditional 316L and SLM 316L. The data of traditional 316L is from public reference.

5. CONCLUSIONS

In this work, several conclusions can be drawn from this work:

1. SLM 316L has higher strength (YS 568 MPa and UTS 693 MPa) and lower ductility (elongation 52%) compared with traditional 316L The high strength is mainly attributed to the (i) cellular substructure, (ii) high dislocation density, and (iii) high content of LAGB, formed by the high cooling rate.
2. The cyclic softening behavior of SLM 316L is mainly attributed to: (i) coarsening of the cellular sub-structure, (ii) texture evolution from <111>∥LD to<001>∥LD, and (iii) decrease of GND density and LAGBs during fatigue.
3. A transgranular fracture mode is observed across a range of strain amplitudes in SLM 316L. At higher strain amplitudes, fatigue cracks are fewer, shorter and wider. The melt boundaries have no obvious effect on resistance or promotion of crack propagation. Fatigue cracks originate from lack-of-fusion defects near the surface of all strain amplitudes. At lower strain amplitudes (0.4%), oxide layer can also act as crack initiation sites.
4. Compared with the traditional 316L, the SLM 316L has larger dispersion in LCF properties and lower reliability at higher strain amplitude. When the strain amplitude is low, the SLM 316L exhibits greater higher reliability.

REFERENCES

Andreau, Olivier, Etienne Pessard, Imade Koutiri, Patrice Peyre, and Nicolas Saintier. 2021. 'Influence of the position and size of various deterministic defects on the high cycle fatigue resistance of a 316L steel manufactured by laser powder bed fusion', *International Journal of Fatigue*, 143.

Benedetti, M., E. Torresani, M. Leoni, V. Fontanari, M. Bandini, C. Pederzolli, and C. Potrich. 2017. 'The effect of post-sintering treatments on the fatigue and biological behavior of Ti-6Al-4V ELI parts made by selective laser melting', *J Mech Behav Biomed Mater*, 71: 295-306.

Blinn, Bastian, Florian Krebs, Maximilian Ley, Roman Teutsch, and Tilmann Beck. 2020. 'Determination of the influence of a stress-relief heat treatment and additively manufactured

surface on the fatigue behavior of selectively laser melted AISI 316L by using efficient short-time procedures', *International Journal of Fatigue*, 131.

Chen, Yefeng, Xiaowei Wang, Jiawei shen, Yawei Peng, Yong Jiang, Xinyu Yang, Sean B. Leen, and Jianming Gong. 2022. 'Deformation mechanisms of selective laser melted 316L austenitic stainless steel in high temperature low cycle fatigue', *Materials Science and Engineering: A*, 843.

Concli, Franco, Lorenzo Fraccaroli, Filippo Nalli, and Luca Cortese. 2021. 'High and low-cycle-fatigue properties of 17–4 PH manufactured via selective laser melting in as-built, machined and hipped conditions', *Progress in Additive Manufacturing*, 7: 99-109.

Elangeswaran, Chola, Antonio Cutolo, Gokula Krishna Muralidharan, Charlotte de Formanoir, Filippo Berto, Kim Vanmeensel, and Brecht Van Hooreweder. 2019. 'Effect of post-treatments on the fatigue behaviour of 316L stainless steel manufactured by laser powder bed fusion', *International Journal of Fatigue*, 123: 31-39.

Hatami, Sepehr, Taoran Ma, Taina Vuoristo, Jens Bertilsson, and Ola Lyckfeldt. 2020. 'Fatigue Strength of 316 L Stainless Steel Manufactured by Selective Laser Melting', *Journal of Materials Engineering and Performance*, 29: 3183-94.

Kumar, Punit, R. Jayaraj, J. Suryawanshi, U. R. Satwik, J. McKinnell, and U. Ramamurty. 2020. 'Fatigue strength of additively manufactured 316L austenitic stainless steel', *Acta Materialia*, 199: 225-39.

Kurzynowski, Tomasz, Konrad Gruber, Wojciech Stopyra, Bogumiła Kuźnicka, and Edward Chlebus. 2018. 'Correlation between process parameters, microstructure and properties of 316 L stainless steel processed by selective laser melting', *Materials Science and Engineering: A*, 718: 64-73.

Pegues, Jonathan W., Michael D. Roach, and Nima Shamsaei. 2019. 'Additive manufacturing of fatigue resistant austenitic stainless steels by understanding process-structure–property relationships', *Materials Research Letters*, 8: 8-15.

Stern, Felix, Jan Kleinhorst, Jochen Tenkamp, and Frank Walther. 2019. 'Investigation of the anisotropic cyclic damage behavior of selective laser melted AISI 316L stainless steel', *Fatigue & Fracture of Engineering Materials & Structures*, 42: 2422-30.

Wang, Xianglong, Jose Alberto Muñiz-Lerma, Mohammad Attarian Shandiz, Oscar Sanchez-Mata, and Mathieu Brochu. 2019. 'Crystallographic-orientation-dependent tensile behaviours of stainless steel 316L fabricated by laser powder bed fusion', *Materials Science and Engineering: A*, 766.

Wang, Y. M., T. Voisin, J. T. McKeown, J. Ye, N. P. Calta, Z. Li, Z. Zeng, Y. Zhang, W. Chen, T. T. Roehling, R. T. Ott, M. K. Santala, P. J. Depond, M. J. Matthews, A. V. Hamza, and T. Zhu. 2018. 'Additively manufactured hierarchical stainless steels with high strength and ductility', *Nat Mater*, 17: 63-71.

Wen, Xinlei, Zhihua Wang, Qiong Wu, and Chengrui Liu. 2019. 'Reliability Analysis for Strain-Based Fatigue Incorporating Dispersity Variation', *IEEE Access*, 7: 180804-17.

Wood, P., T. Libura, Z. L. Kowalewski, G. Williams, and A. Serjouei. 2019. 'Influences of Horizontal and Vertical Build Orientations and Post-Fabrication Processes on the Fatigue Behavior of Stainless Steel 316L Produced by Selective Laser Melting', *Materials (Basel)*, 12.

Wu, L., S. R. Agnew, Y. Ren, D. W. Brown, B. Clausen, G. M. Stoica, H. R. Wenk, and P. K. Liaw. 2010. 'The effects of texture and extension twinning on the low-cycle fatigue behavior of a rolled magnesium alloy, AZ31B', *Materials Science and Engineering: A*, 527: 7057-67.

Xie, Liyang, Jianzhong Liu, Ningxiang Wu, and Wenxue Qian. 2014. 'Backwards statistical inference method for P–S–N curve fitting with small-sample experiment data', *International Journal of Fatigue*, 63: 62-67.

Zhang, Hongzhuang, Mengtao Xu, Zhendong Liu, Changyou Li, and Yimin Zhang. 2021. 'Role of local recrystallization behavior on fatigue performance of SLMed 304L austenitic stainless steels', *Materials Characterization*, 177.

Zhang, Yinling, Xiaoying Fang, Hongtao Wang, Ran Zong, Ertuan Zhao, Jinguo Han, Zhichao Dong, and Zhixiong Zhang. 2022. 'Microstructure and low-cycle fatigue performance of selective electron beam melted Ti6Al4V alloy', *International Journal of Fatigue*, 163.